AIChE

Assembly of Uniform Photoluminescent Microcomposites Using a Novel Micro-Fluidic-Jet-Spray-Dryer

Winston Duo Wu, Ria Amelia, Na Hao, and Cordelia Selomulya
Dept. of Chemical Engineering, Monash University, Clayton, VIC 3800, Australia

Dongyuan Zhao
Dept. of Chemistry, Laboratory of Advanced Materials, Fudan University, Shanghai, P.R. China

Yu-Lung Chiu
School of Metallurgy and Materials, The University of Birmingham, Edgbaston Birmingham B15 2TT, U.K.

Xiao Dong Chen
Dept. of Chemical Engineering, Monash University, Clayton, VIC 3800, Australia; and Dept. of Chemical and Biochemical Engineering, College of Chemistry and Chemical Engineering, Xiamen University, P. R. China

DOI 10.1002/aic.12489
Published online January 19, 2011 in Wiley Online Library (wileyonlinelibrary.com).

Generation of uniform micro-particles containing (i) pure lactose; (ii) silica nanoparticles and lactose; (iii) silica nanoparticles/lactose doped with Eu(III) have been successfully achieved using a novel spray dryer with a uniquely designed microfluidic aerosol nozzle as the monodisperse droplet generator. Here we investigate the impacts of precursor compositions and concentrations, as well as the drying temperature profile on particle size, morphology, and surface element distribution. Distinct morphologies are observed with different precursor compositions, ranging from smooth spherical lactose microparticles to the buckled shape for composites containing silica nanoparticles. The formation of such morphology is qualitatively interpreted by using Peclet number, indicating that the presence of the suspended silica nanoparticles facilitates shell formation at the early stage of the drying process. As the drying continue, such shell is subject to buckling, induced by the capillary force due to the lower mechanical integrity inside the droplet. Post calcination, transmission electron micrographs of Eu(III)/silica nanoparticles/lactose microcomposites confirm the formation of nano-sized Eu_2O_3 homogeneously embedded on the silica shell. Photoluminescence spectra of these particles indicate that enhancement of photoluminescence intensity is directly related to the europium loading, which could be adjusted from the precursor composition. This work demonstrates a scalable route to assemble relatively complex composites with uniform properties, without extensive conjugation or purification steps commonly required in wet chemistry-based processes. *AIChE J*, 57: 2726–2737, 2011
Keywords: monodisperse, microcomposites, surface morphology, spray drying, silica nanoparticles

Correspondence concerning this article should be addressed to X. D. Chen at dong.chen@eng.monash.edu.au or xdc@xmu.edu.cn.

Introduction

Solid particles or microcomposites containing rare earth metal ions such as Y^{3+}, Ce^{3+}, Nd^{3+}, and Eu^{3+} have attracted

great interest due to their distinct properties and applications in luminescence,[1–5] catalysis,[6–8] and magnetism.[9–11] To optimally realize their functionalities, some degree of control over characteristics such as particle size, size distribution, morphology, and surface composition is required. For instance, higher luminescent yield and packing density can be achieved for nonagglomerated spherical particles of the luminescent materials.[12] Often silica is used as lattice or support materials for the luminescent components due to its dispersibility in aqueous suspension and stable chemical and physical properties.[13–16] Various methods including sol-gel,[5,13,17] homogeneous precipitation,[14,18] functionalization,[19,20] and spray drying/spray pyrolysis[12,16,21–24] to produce photoluminescent microparticles have been reported. Both spray drying and spray pyrolysis generate particles by converting atomized liquid droplets into solids, although spray drying operates on a much lower temperature range (<400°C), with further calcination step required to produce crystalline structures. The advantages over wet chemistry routes include avoiding the use of excessive solvents/chemicals, ability to operate continuously and often without the need of any purification or separation steps, with the possibility to assemble a range of functional composites.

Conventional spray dryers suffer from poor controllability on particle characteristics and functionalities due to the size polydispersity of the atomized droplets, causing the droplets to undergo different evaporation processes despite the same drying environment.[25] The complex spray traveling trajectories of different-sized droplets often result in undesirable agglomeration.[23,24] To generate uniform spray-dried particles, the generation of monodisperse droplets is necessary, coupled with re-designing the dryer component to convert the droplets into particles without coalescence among the droplets or semidried particles. In this work, a novel spray dryer referred to as the Micro-Fluidic-Jet-Spray-Dryer (MFJSD) has been used to prepare uniform, nonagglomerated micro-composites containing (i) pure lactose; (ii) silica nanoparticles and lactose; (iii) silica nanoparticles/lactose doped with Eu(III). Monodisperse droplets of the liquid precursors were generated using a specially fabricated Micro-Fluidic Aerosol Nozzle (MFAN). We investigated the impacts of different compositions and concentrations of the precursors and various drying temperature profiles on the size, morphology, surface structure, element distribution, and the photoluminescence of europium-doped composites. The study demonstrated the potential of this new spray drying method to generate complex composites with controlled characteristics at a much lower temperature range than commonly encountered in conventional dryers, due to the efficient contact between each individual droplet and the drying air. This opens up the possibilities of using the technology to assemble other heat sensitive or bioactive materials where temperature is usually the deciding factor in determining the appropriate synthesis route.

Experimental

Materials

Distilled water (18.2–18.3 MΩ cm^{-1}) was used to prepare aqueous solution. Europium (III) chloride (anhydrous $EuCl_3$, 99.9+% trace metals basis) powder, α-lactose monohydrate powder ($C_{12}H_{22}O_{11}.H_2O$) and Ludox®-LS colloidal silica sol (30 wt % in water, ± 7 nm) were purchased from Sigma-Aldrich (AUS). All chemicals were reagent grade and used without further purification. Five different compositions of the precursor solutions for spray drying were prepared (Table 1). Silica nanoparticles were added by diluting appropriate amounts of silica sol into 500 mL of water. $EuCl_3$ and lactose powders were dissolved into the aqueous solution to prepare precursors with different europium contents (SLE). For comparison, solutions containing only lactose (L) and lactose/silica nanoparticles (SL) were also prepared.

Table 1. Precursor Solution Composition

Sol	Silica (g)	Eu(III) (Atom % Based on Silica)	Lactose (g)
L	0	0	2
SL	0.3	0	2
SLE1	0.3	1%	2
SLE2	0.3	2%	2
SLE3	0.3	8%	2

Monodisperse droplet formation and droplet size measurement

The precursor solution was poured into a 1.5 L standard steel reservoir and atomized using the MFAN atomizing system, as illustrated in Figure 1a with Figure 1b showing the schematic structure of MFAN. The detailed study on the theory and application of the MFAN system to form monodisperse droplets can be found in the authors' previous paper.[25] In brief, a glass tube surrounded by a piezoelectric annular component and connected to a pulse generator (Microfab Technologies) was controlled using a computer. A glass capillary with a given radius (r_j) served as the orifice of MFAN, while the orifice diameter of the nozzle was 75 μm. To form monodisperse droplets, dehumidified instrument air was used to force the liquid in the reservoir to jet through the nozzle. The liquid jet was broken into droplets by regular squeezing of the glass tube using a piezoelectric component with a sinusoidal electrical signal of frequency (f_{set}) transferred from the pulse generator. The jet velocity (v_j) was controlled by adjusting the back-pressure of the reservoir, and was calculated as $v_j = v_m/\pi r_j^2$, with ρ and v_m representing the density of the liquid (kg m^{-3}) and the mass flow rate (kg s^{-1}) respectively—both of which were experimentally measured. To investigate the droplet formation process (i.e., jet diameter, droplet spacing, size, and size distribution), photographs were taken using a digital SLR camera (Nikon, D90) with a speed-light (Nikon SB-400) and a micro-lens (AF Micro-Nikkon 60 mm f/2.8D). The software of image processing and analysis in Java (ImageJ™) was used to analyze the photographs. Figure 2 shows the photographs taken for monitoring the droplet formation process and measuring the droplet size and size distribution with relative error of less than 2%. The droplet diameters were 142 ± 2.7 μm, 156 ± 2.3 μm, 154 ± 2.3 μm, 157 ± 2.5 μm, and 154 ± 2.4 μm, respectively, for samples L, SL, SLE1, SLE2, and SLE3, with no notable size differences between the individual droplets. The measured droplet size was approximately twice the orifice diameter, in good agreement with the classic Rayleigh's theory.[26] The lactose droplets were smaller than those generated from the rest of the compositions,

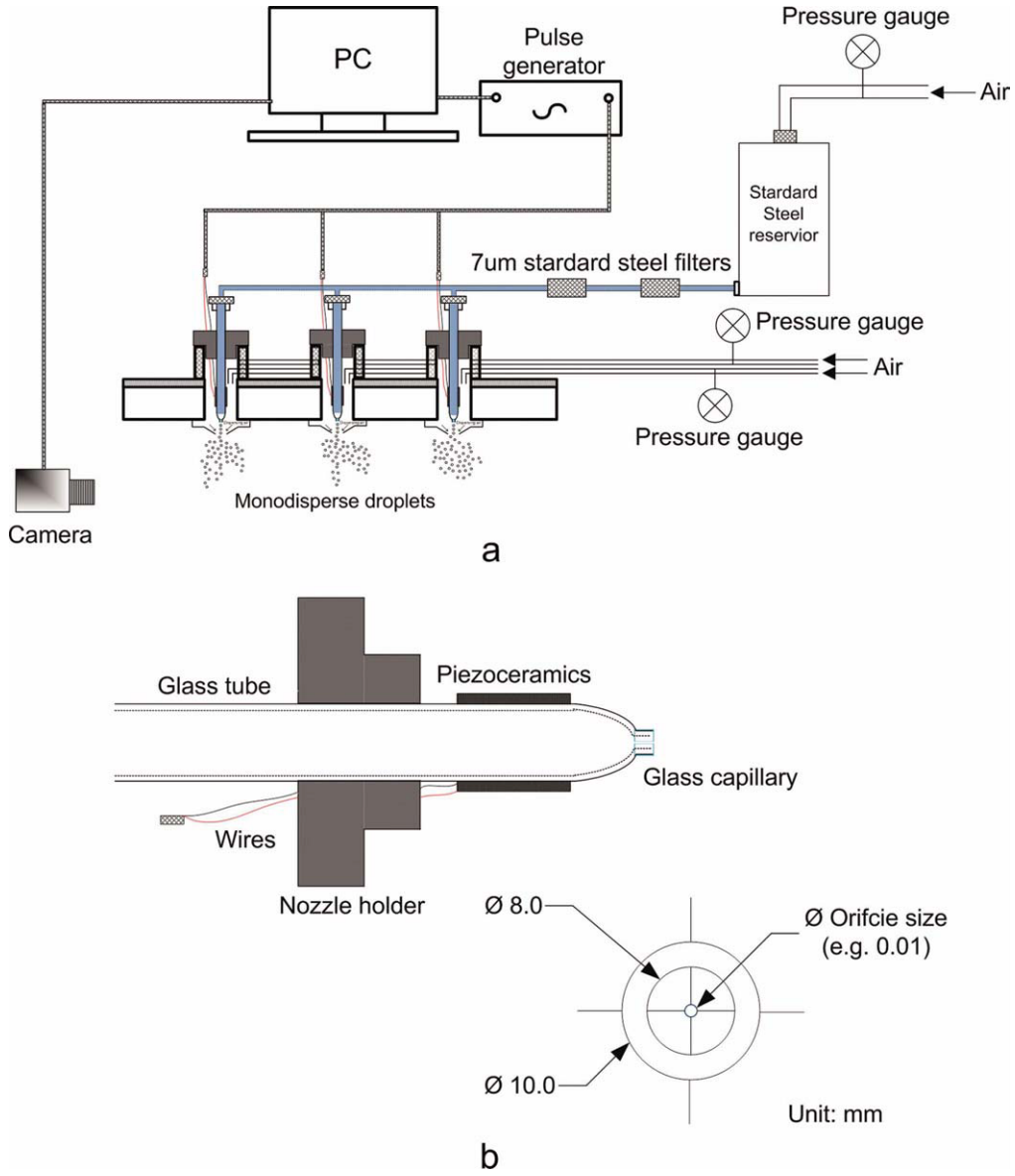

Figure 1. (a) Home-made MFAN atomizing system. (b) Schematic graph of MFAN structure.

[Color figure can be viewed in the online issue, which is available at wileyonlinelibrary.com.]

likely due to the lower viscosity of the lactose solution than when silica nanoparticles were present in the precursor solution. The droplet generation could be stably maintained for more than 5 h, ensuring a continuous production rate.

Fabrication of uniform microcomposites

The schematic of the MFJSD is shown in Figure 3. The dryer chamber was made of a zinc cylinder with the upper part (2000 mm) insulated by double asbestos layers. The diameter and height of the cylinder chamber were 600 and 3000 mm, respectively. Four hot air guns (PHG 630 DCE, Bosch, Australia) were assembled on a hot air dispenser on the top of the dryer. The air-flow could be set in three steps for 150, 300, 500 L/min, respectively. The heating temperature range could be controlled from 50 to 630°C by the interval of 10°C. Six thermocouples were attached to the dryer chamber to monitor drying temperature distribution, with a humidity sensor to measure the relative humidity at the dryer outlet. The hot air dispenser as shown in Figure 3 (inset) was composed of two zinc sheets connected using rivets. The diameter of the sheet above and below was 700 and 590 mm, respectively, with the gap of 120 mm. The sheet above covered the top of the dryer chamber while the one below has 5 mm drilled holes to evenly dispense the hot air from the hot air guns into the dryer chamber. Different set-temperatures of the hot air guns were applied to realize the various drying temperature profiles inside the dryer chamber, with Figure 4 depicting the temperature profiles used in this work. The

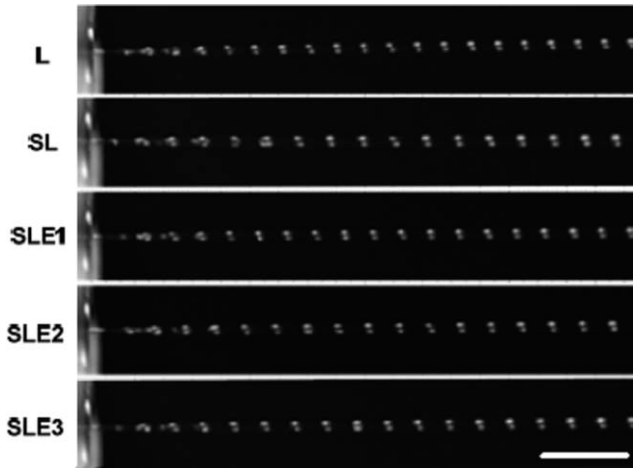

Figure 2. Photographs of droplet generation for sample L, SL, SLE1, 2, and 3 (Scale bar: 1mm).

spray-dried particles were collected in a filter bag at the bottom of the dryer. The spray-dried particles were stored in the desiccator with the environment temperature of 25°C before the particle characterization. The samples containing Eu(III) were further calcined at 1000°C for 3 h.

Particle characterization

Information on particle size, size distribution, and morphology were obtained from the images taken by a field emission scanning electron microscope (FESEM, 7001F, Japan). FESEM energy dispersive X-ray photoelectron spectrometer (XPS) was conducted to verify the presence of chemical elements, distributions, and their relative amounts at less than 5 nm below the particle surface. Energy dispersive X-ray elemental mapping and high resolution TEM were conducted to confirm the presence of europium oxide nanoparticles after calcination of the spray-dried samples. The phase composition of particles was

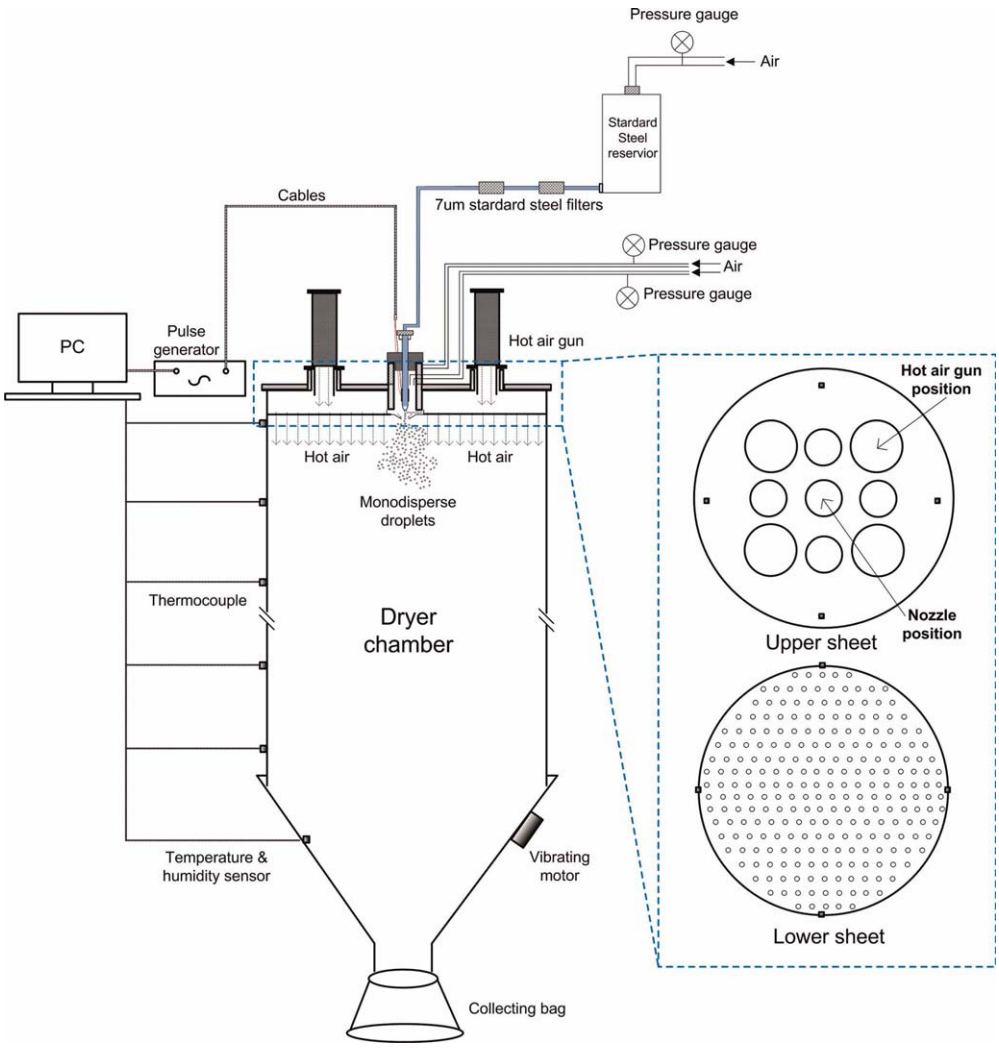

Figure 3. A schematic graph of the front view of the MFJSD.

[Color figure can be viewed in the online issue, which is available at wileyonlinelibrary.com.]

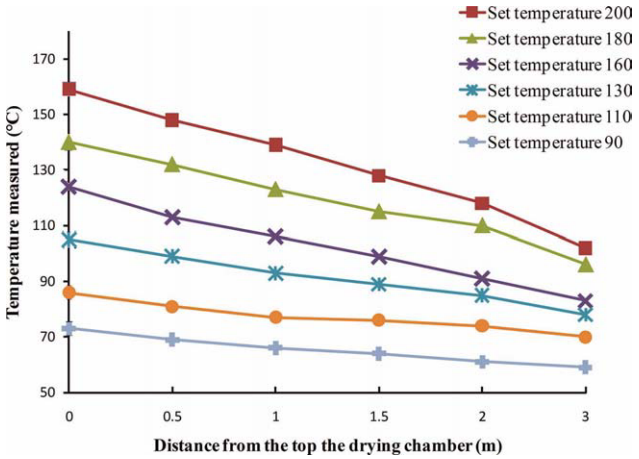

Figure 4. Various drying temperature profiles inside the dryer chamber of the MFJSD using different set-temperatures of the hot air guns.

[Color figure can be viewed in the online issue, which is available at wileyonlinelibrary.com.]

examined by a Holland Philips 1130 X-ray diffractometer (XRD) with Ni-filtered Cu Kα radiation (40 kV, 25 mA). Fourier transform infrared (FTIR) spectra were obtained using a FTIR360 spectrometer with a resolution of 2 cm^{-1} in the wavelength range of 400–4000 cm^{-1} using KBr pallet to confirm the presence of specific elemental bonds. The photoluminescence properties of the calcined SLE particles were quantified by a fluorescence spectroscopy at 20°C at a resolution of 3 nm.

Results and Discussion

Assembly of nonagglomerated, uniform lactose particles

The lactose-only solution was spray-dried at set-temperatures of 110, 130, and 160°C. FESEM images (Figure 5) show that the lactose particles were of uniform size with discrete, spherical morphology and relatively smooth surface. The average diameters based on analysis of over 1500 particles for L-160, L-130, and L-110 were 44.57 $\pm$ 0.37 μm; 44.35 $\pm$ 0.35 μm; and 42.10 $\pm$ 0.36 μm, respectively (Figure 6), indicating very narrow size distributions. The uniformity in size and morphology of the particles suggested that every

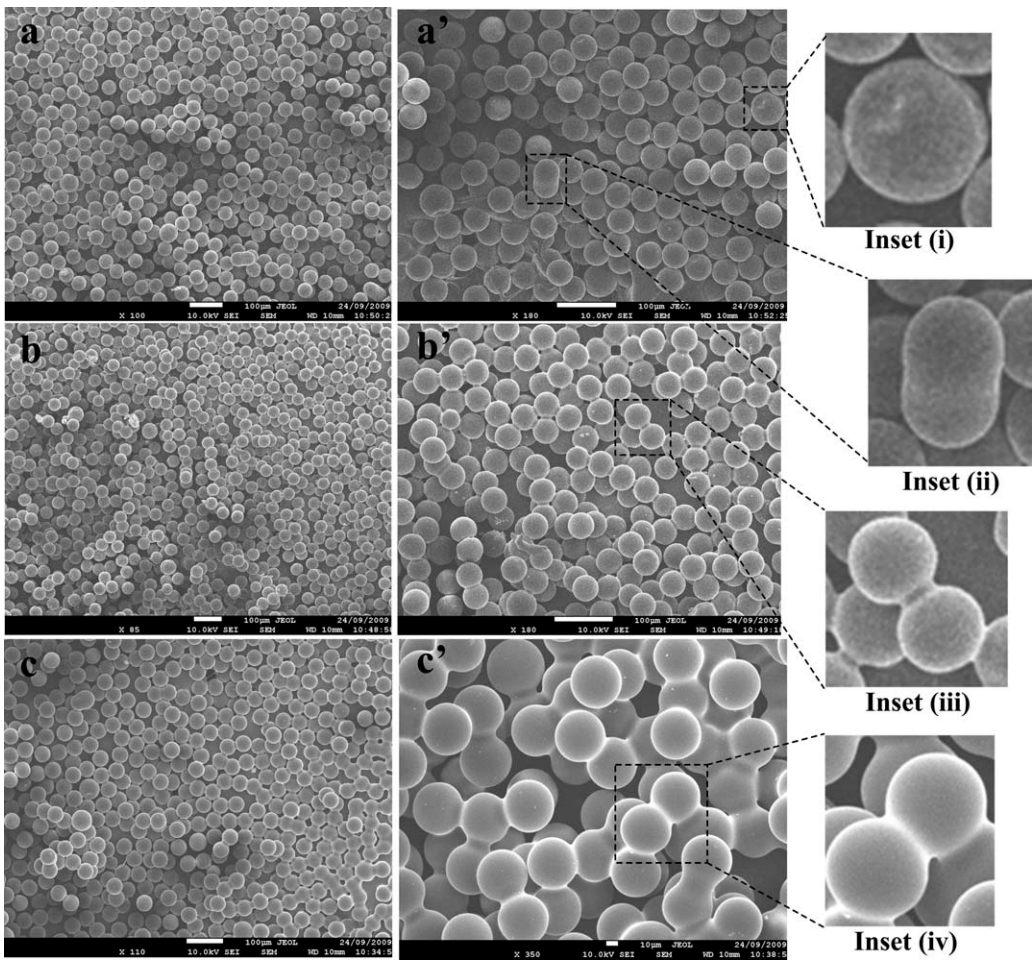

Figure 5. FESEM images of spray-dried lactose particles: (a & a′) L-160; (b & b′) L-130; and (c & c′) L-110. Inset (i) showing larger particle than average, while inset (ii) displays conjoined particles; Insets (iii & iv): particles with bridging adhesions.

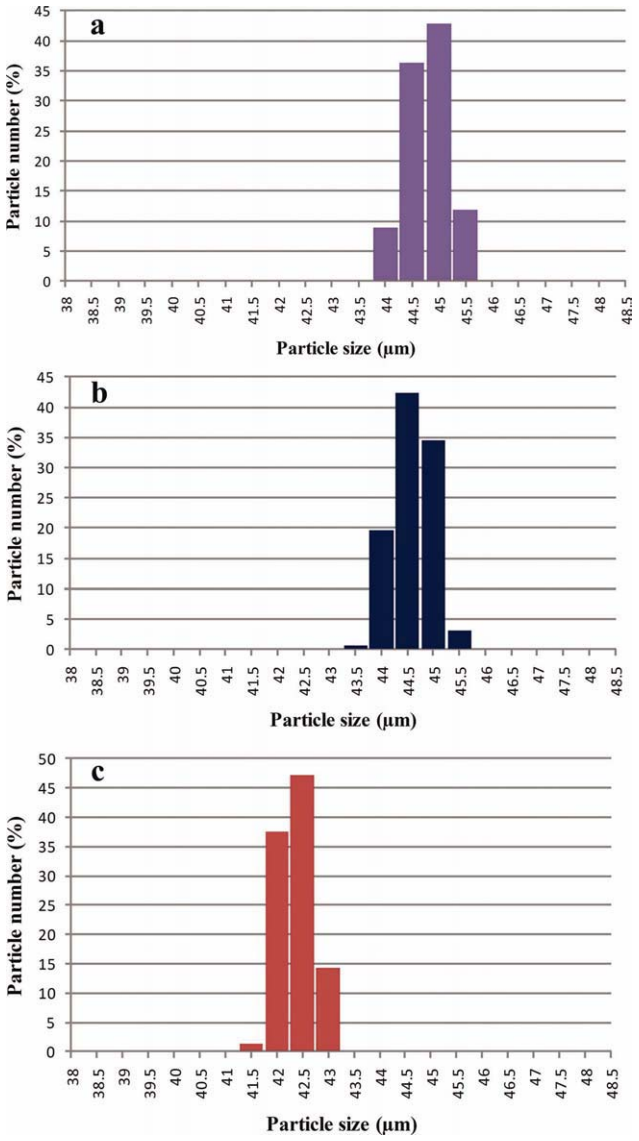

Figure 6. Size distributions of spray-dried lactose particles: (a) L-160; (b) L-130; and (c) L-110.

[Color figure can be viewed in the online issue, which is available at wileyonlinelibrary.com.]

individual droplet generated by the atomizer experienced similar evaporation process in the dryer chamber, and the majority of the droplets were dried into particles in one-to-one relationship.

There were several circumstances of coalescence among droplets and semidried particles, resulting in either slightly larger particle size (Figure 5, inset (i)) or conjoined doublets (Figure 5, inset (ii)). With lower drying temperature, there was no significant difference between the average particle size or size distribution, but the moisture content of the dried samples was found to increase from 8, 12, and 15% for L-160, L-130, and L-110, respectively. The lower drying temperature induced higher particle moisture content and larger degree of fusion between neighboring particles (Figure 5, insets (iii, iv)). Such phenomenon could be possibly explained by investigating the effect of the residual moisture on the glass transition temperature of the spray dried lactose particles. These particles are amorphous as verified by XRD analysis (Figure 12) which behave as solid when stored at a temperature well below their glass transition. However, any residual moisture would act as a plasticizer decreasing the glass transition. When the glass transition is decreased below the storage temperature, the amorphous material would behave as viscous liquid, likely causing particle fusion.[27] Based on the reported values for the glass transition of spray dried lactose as a function of water content, the particles generated in this work with 8, 12, and 15% water content corresponded to glass transition temperature of 50, 20, and 4°C, respectively. Clearly, the amorphous lactose particles with glass transition temperatures below the storage temperature of 25°C were more prone to behave as viscous liquid that induced fusion between the particles.

Assembly of microcomposites containing silica nanoparticles

Precursor solutions containing silica nanoparticles (SL) were spray dried at set-temperatures of 110, 130, 160, 180, and 200°C. FESEM images of the resulting composites display similar morphology (Figure 7), indicating that in this study drying temperature has little effects on the dry particle shapes. The SL composites were buckled and crumpled, distinctive from the spherical lactose particles (Figure 5) with relatively smooth surface produced in a similar drying condition. Given the identical composition of the precursor solution and the same initial droplet size, the average SL particle size slightly increased with drying temperature above 160°C (Figure 8). The reason for this could be that at a high drying temperature, the droplets could quickly form a skin that resisted further shrinkage to form larger particles, consistent with the previous work.[28]

The structure of spray-dried particles is determined by the properties of materials composing the precursor solution, the initial droplet size, and the spray drying conditions. A couple hypotheses were offered previously to explain the formation of the SL composite structures, namely (i) the deformation of the droplets resulted from up-flowing hot air stream and (ii) the presence of colloidal silica nanoparticles in the precursor solution. Iskandar et al.[24] proposed that droplets of large size were subject to the impact of airflow inside the dryer chamber, and thus the droplets were unable to maintain the initial spherical shape, resulting in irregular dry particles. However, the wide size distribution of both the droplets and dry particles, and the extent of particle agglomeration in their particular study rendered it difficult to obtain a direct correlation with the drying conditions. In our work, the initial droplets were monodisperse, and approximately the same size even for different precursor solutions (Figure 2), and each droplet was individually dried into a single particle. Given that the dry lactose particles had spherical morphology, verifying that the droplets could indeed maintain their shape, the influence of droplet deformation in this case could be excluded as the main reason for the irregular shapes observed for SL microcomposites assembled in similar drying conditions.

Looking at the impact of silica nanoparticles, previous investigations[29-31] have demonstrated the buckling and crumpling behavior of drying a droplet containing colloidal

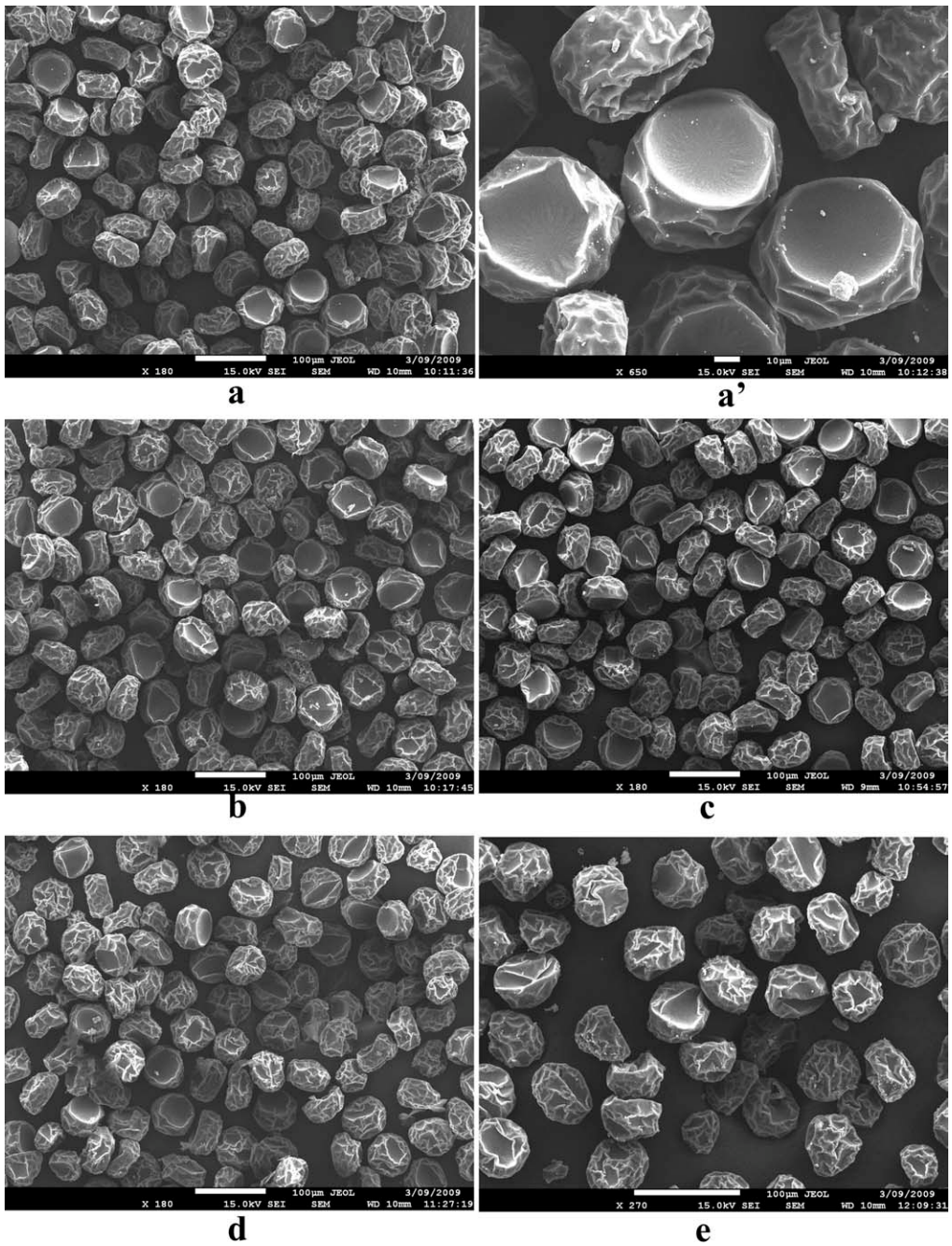

Figure 7. FESEM images of (a) SL-200; (a′) SL-200 in a higher magnification; (b) SL-180; (c) SL-160; (d) SL-130; (e) SL-110.

nanoparticles using the single droplet drying experiment. This morphology deformation have been interpreted as follows: in the initial drying period, the droplet surface recedes isotropically while the surface is concentrated by the suspended nanoparticles that gradually form a shell before the drying process is completed. The droplet continues to shrink as the shell thickens. As drying progresses, the nanoparticles are eventually packed close enough while being stabilized by the electrostatic inter-particle forces to resist further shrinkage. The solvent, however, continues to evaporate, thus exerting compressive capillary stresses on the particle surface, when overcoming the electrostatic forces, to cause the surface to buckle.[30] The fundamental mechanism of the particle deformation could be correct. However, the single droplet drying scheme is different from spray drying in many aspects. For example, the studies on single droplet drying[29,32] are usually done with the droplet in the sub-millimeter diameter range and the entire drying period takes tens of seconds, while the realistic size of the droplets in spray drying is usually below tens of microns with much shorter

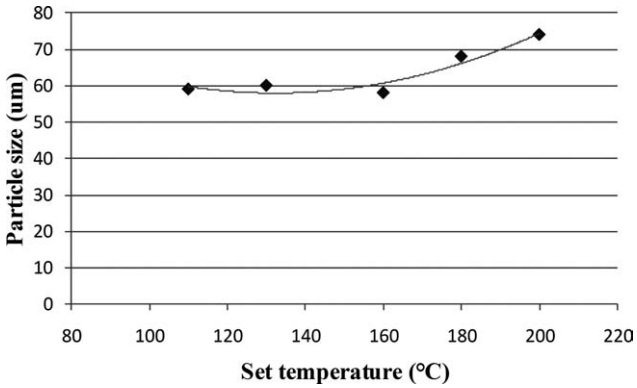

Figure 8. Average size of silica nanoparticles/lactose (SL) composites assembled under different spray drying temperatures.

processing time-scales. Additionally the single droplet drying is performed within a relatively static environment, whereas the temperature field and flow field in the vicinity of the droplet are varied along the spray dryer chamber where the droplets travel.[28]

To investigate the morphology formation of spray dried particles, it would be ideal to obtain uniform particles by restricting the droplet size range and controlling the spray drying conditions. Otherwise the formation mechanism can hardly be derived from polydisperse particle size and morphology even within the same batch. Few studies[28,33,34] used modified small-scaled spray dryers to produce fairly homogeneous particles, and suggested that Peclet number (*Pe*) can be used as a guide to characterize the morphology of spray dried particles. *Pe* is defined as the ratio between droplet evaporation rate and solute(s) diffusion rate:

$$Pe = \frac{\frac{\partial r_d}{\partial t} \cdot r_d}{D_s}$$

Where r_d is the droplet radius, $\partial r_d/\partial t$ is the rate of change of the droplet radius, and D_s is the diffusion coefficient of the solutes inside the droplet.

In this study, as qualitatively shown in Figure 9, regardless of the droplet compositions, the diffusion rate of the solutes inside the droplet decreased while the drying proceeded due to the declining diffusion coefficient.[34] The evaporation rate also fell due to increasing difficulty in removing the residual moisture. Both SL droplet and the neat lactose droplet experienced initially isotropical drying period (t_i). As the droplet kept shrinking, a shell is gradually formed on the surface. The time of such shell formation (t_s) for SL droplet could be shorter than for the lactose droplet, i.e., $t_s(SL) < t_s(L)$ due to the existence of suspended silica nanoparticles whose diffusion coefficient was much smaller than the lactose molecules (with high *Pe*). Thus the silica nanoparticles accumulated faster at the surface to form a shell, preventing further shrinkage of the droplet.[30] In contrast, the diffusion rate of the lactose molecule was faster or at the same order as the droplet evaporation rate (referred to as low *Pe*), and hence the surface precipitation was expected to appear later during the drying process. This difference in the onset time of the shell formation was evidenced by the larger SL particle size than the lactose particle produced with the similar droplet size and the same spray drying conditions. With continuing evaporation, the SL semidried particle was subject to buckling at t_b when the electrostatic forces were secondary to the capillary force because of the deficient internal mechanical integrity resulted from relatively slow solute re-distribution.[27] In comparison, the dried lactose particle was able to maintain spherical with smooth surface. This could be ascribed to the larger diffusion rate of the lactose molecules resulting in faster re-homogenization throughout the droplet, leading to the better mechanical integrity of the lactose shell formed at the characteristic time (t_s(L)) close to the droplet lifetime (t_d).[34]

Assembly of Eu-doped microcomposites

Precursor solutions containing europium were spray-dried at set-temperature of 110, 130, 160, 180, and 200°C. Figure 10 displays the FESEM images of SLE1, SLE2, and SLE3 particles spray dried at 130°C, indicating relatively dense particle surface without visible pores. The particles have similar morphology as the SL composites containing silica nanoparticles, with equivalent mean particles size at the same drying temperature, indicating that the addition of $EuCl_3$ in the precursors had little impact on the morphology or size. FESEM EDXPS of these particles (Figure 11) indicate the increase of Eu(III) signal with its content in the precursor solution, with the signals from Eu(III) and silica evenly distributed in the entire particle domain. Silica nanoparticles may act as seeds and interact with Eu(III) to form homogeneous network of Eu(III)-silica composites. XRD patterns (Figure 12) of lactose particles (L) assembled at 130°C exhibits one broad diffraction at 2θ angles of ~20°, indicating amorphous structure with little or no crystallization. Both SL and SLE particles show similar XRD patterns, suggesting amorphous hybrid composites. Comparatively, calcination of the spray-dried sample caused the formation of crystalline oxides, as indicated by the XRD pattern of the calcined SLE3 (Figure 12). Three typical peaks shown at $2\theta = 28.91$, 32.88, and 47.18° indicate the presence of Eu_2O_3.

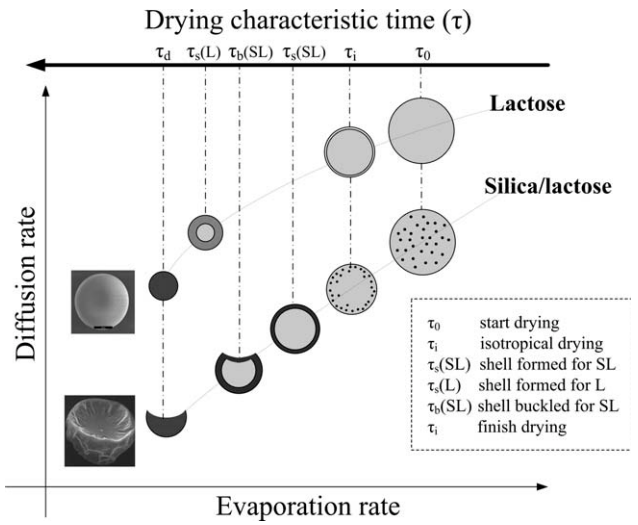

Figure 9. Proposed drying stages undergone by droplets composed of lactose and lactose with silica nanoparticles, related to their final morphologies.

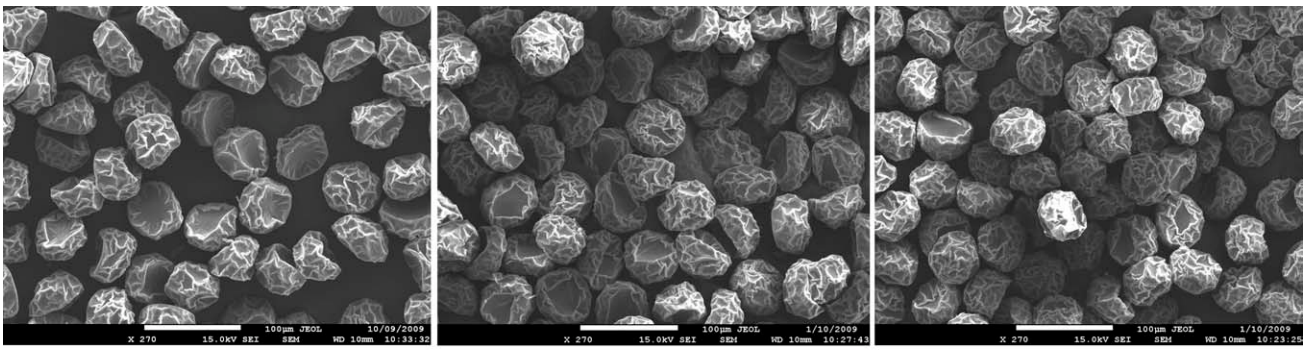

Figure 10. FESEM images of (a) SLE1; (b) SLE2; (c) SLE3 assembled under a set temperature of 130°C.

High resolution TEM image (embedded in Figure 13) of the calcined SLE3-130 sample confirmed the crystalline structure. It is noticeable that a number of black dots, possible appearance of nano-Eu_2O_3 (~20 nm) homogeneously locate inside the composite matrix. TEM EDXPS results (Figure 13) verified this composite structure by displaying that the europium

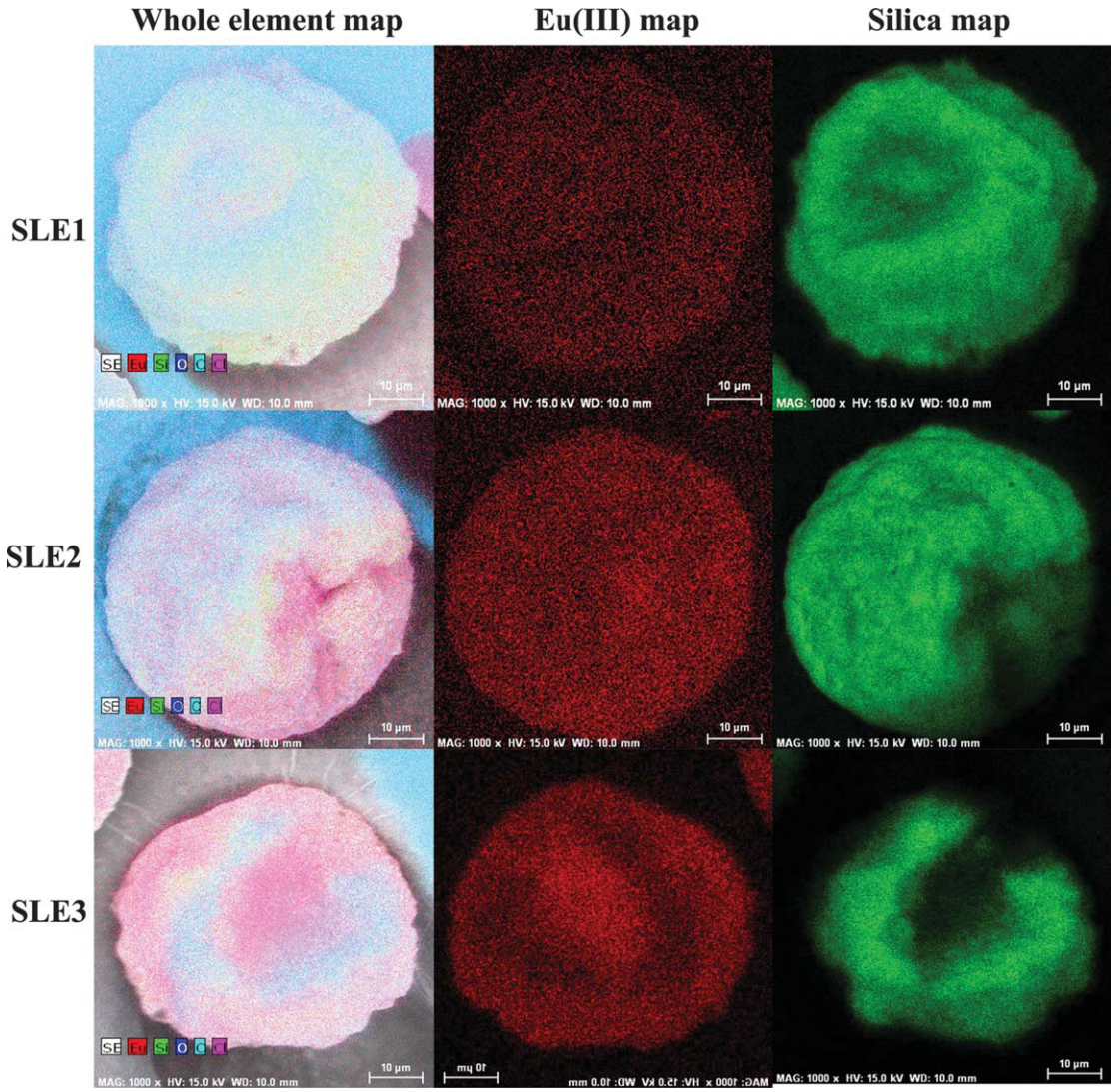

Figure 11. FESEM energy dispersive XPS of SLE1, SLE2, and SLE3 composites assembled at 130°C (prior to calcination).

[Color figure can be viewed in the online issue, which is available at wileyonlinelibrary.com.]

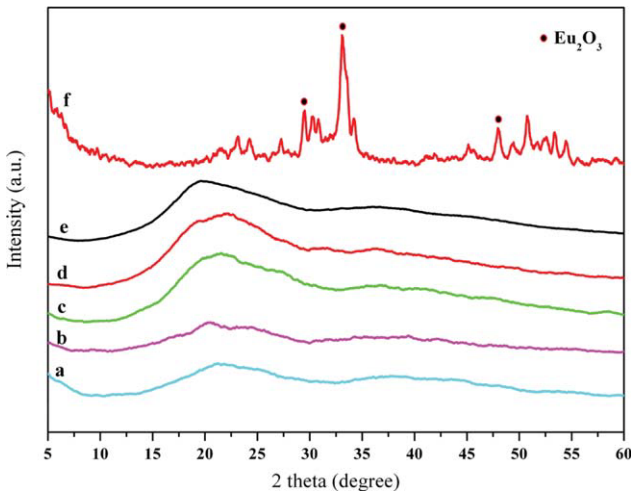

Figure 12. High-angle XRD patterns of (a) L; (b) SL; (c) SLE1; (d) SLE2; (e) SLE3 spray-dried at 130°C showing amorphous structures; and (f) SLE3 post-calcination showing peaks attributed to europium oxide.

[Color figure can be viewed in the online issue, which is available at wileyonlinelibrary.com.]

concentration, as measured using the Lα1, showed a consistency with the small particles embedded in the matrix, whereas the silicon almost covered the whole mapped area. This result is also in consistence with the EDXPS analysis of the as-synthesized sample (Figure 11), indicating that the calcination may not destroy the basic composite structure.

FTIR characterization

FTIR spectra (Figure 14a) of spray-dried lactose particles show one band at 3380 cm^{-1}, due to the stretching vibrations of O—H bonds.[35,36] The band at 2931 cm^{-1} was due to the stretching vibrations of C—H bond, while the weak band at ~1655 cm^{-1} corresponded to the stretching vibrations of the physical water adsorbed.[28,36] The band at ~712 cm^{-1} was attributed to C—C vibrating and stretching originating from ring-deformation motions of cyclic hydrocarbon. The band at ~1414 cm^{-1} was due to the bending vibrations of C—H bonds, while at 1118 cm^{-1} was caused by the asymmetrical stretching vibrations of C—O—C ether unit bonds.[28,37] The peak at 788 cm^{-1} was from the C—H deformation motions out of the ring plane, where the vibrations of the lactose molecule appeared.[28,35,36]

After adding colloidal silica nanoparticles, the FTIR spectra of the SL (Figure 14b) and SLE1-SLE3 (Figures 14c–e) showed bands at ~1118 cm^{-1} and ~887 cm^{-1}, indicating Si—O—Si stretching and Si—OH vibration, respectively.[38] Comparatively, FTIR spectra (Figures 14c–e) of the SLE samples containing different Eu(III) contents prior to calcination showed one strong band at ~480 cm^{-1} probably from Eu—O stretching mode. This indicates that Eu^{3+} ions might be

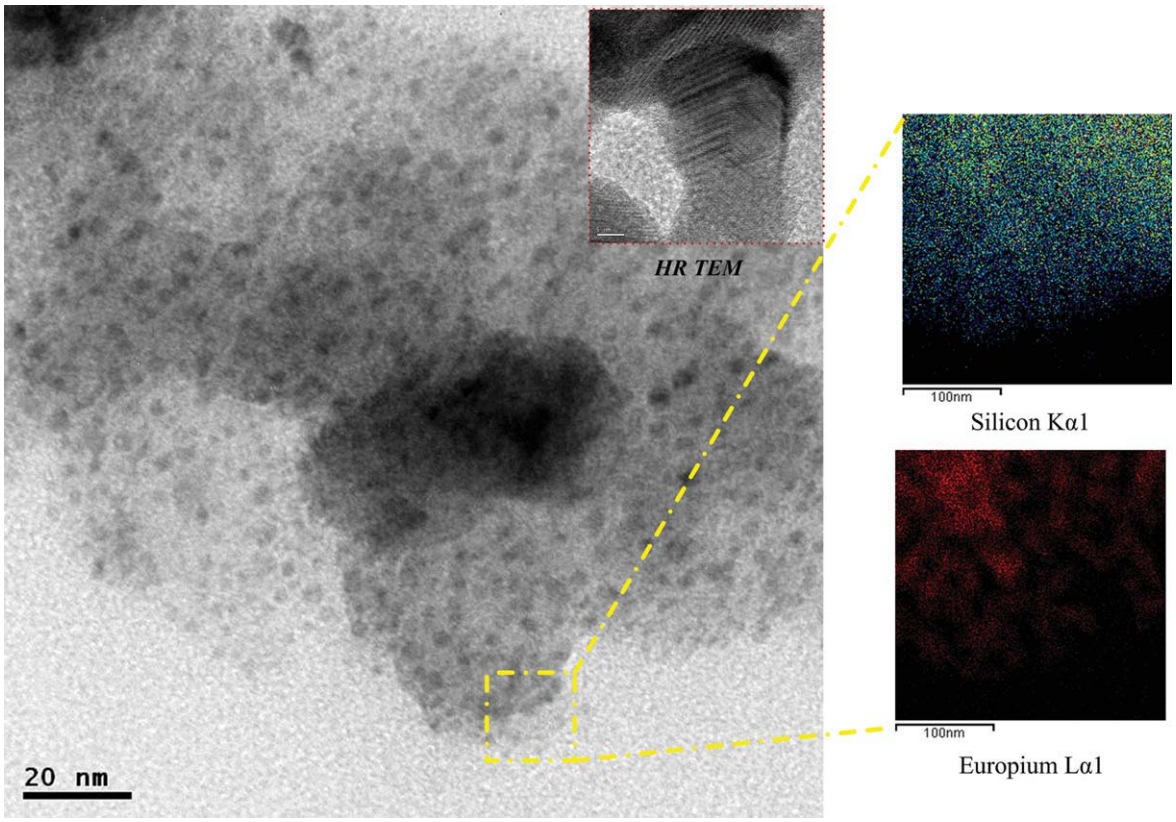

Figure 13. TEM image and EDXPS of the calcined SLE3-130 sample.

[Color figure can be viewed in the online issue, which is available at wileyonlinelibrary.com.]

incorporated through oxygen atoms within the silica matrix. The relatively strong affinity of Eu(III) ions to the hydroxyl groups on the silica surface may result in the formation of Eu—O—Si.[39] The calcined SLE3 sample also showed bands at ~1118 cm^{-1} and ~480 cm^{-1} (Figure 14f), indicating Si—O—Si and Eu—O bonds, in agreement with XRD and energy dispersive X-ray elemental mapping data.

Photoluminescence properties

XRD data (Figure 12f) confirmed the presence of europium oxide on the calcined sample (SLE3). The emission spectra of calcined samples of SLE assembled at different drying temperatures and at different Eu contents under excitation at 394 nm are shown in Figure 15. The characteristic peak of Eu(III) at approximately 612 nm were observed in all cases due to the red 5D0 → 7F2 transition at C2 sites within europium.[40,41] Another peak appeared at ~592 nm from the 5D0 → 7F1 transition.[13,21] Emission spectra of samples spray-dried at different temperatures (Figure 15a) demonstrated negligible impact of spray drying temperatures on the photoluminescence property. Iskandar et al.[24] previously showed that the photoluminescence intensity of particles with identical composition and similar size was dependent on the spray pyrolysis temperature. However, this could be ascribed to the pyrolysis process itself with temperature variation from 400 to 1200°C that could significantly influence the particle characteristics, especially the degree of crystallinity and the crystalline size, as well as the distribution of the photoluminescence element throughout the structure. In our case, both FESEM and XPS analyses have revealed no distinct structural differences between particles assembled by the spray drying method within the actual drying temperature of <180°C, while the Eu(III) ions were homogeneously located on the particle surface for all cases (Figure 11) attributing to similar photoluminescence property. On the other hand, increasing Eu(III) content (Figure 15b) enhanced the relative photoluminescence intensity related to the increase of concentration in the precursor solution.

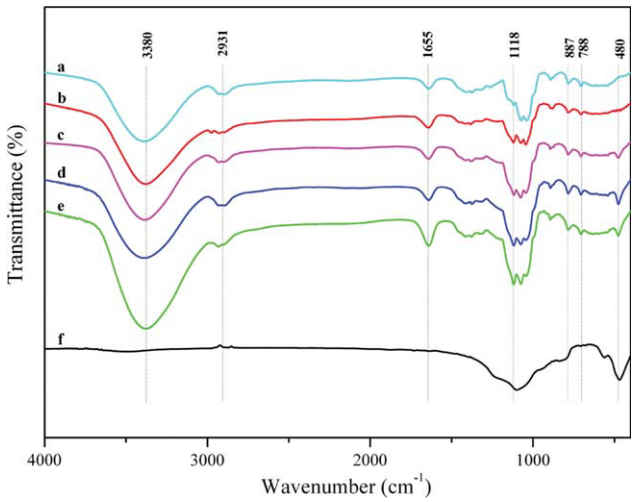

Figure 14. FTIR spectra of (a) L; (b) SL; (c) SLE1; (d) SLE2; (e) SLE3 assembled at 130°C; (f) calcined SLE3.

[Color figure can be viewed in the online issue, which is available at wileyonlinelibrary.com.]

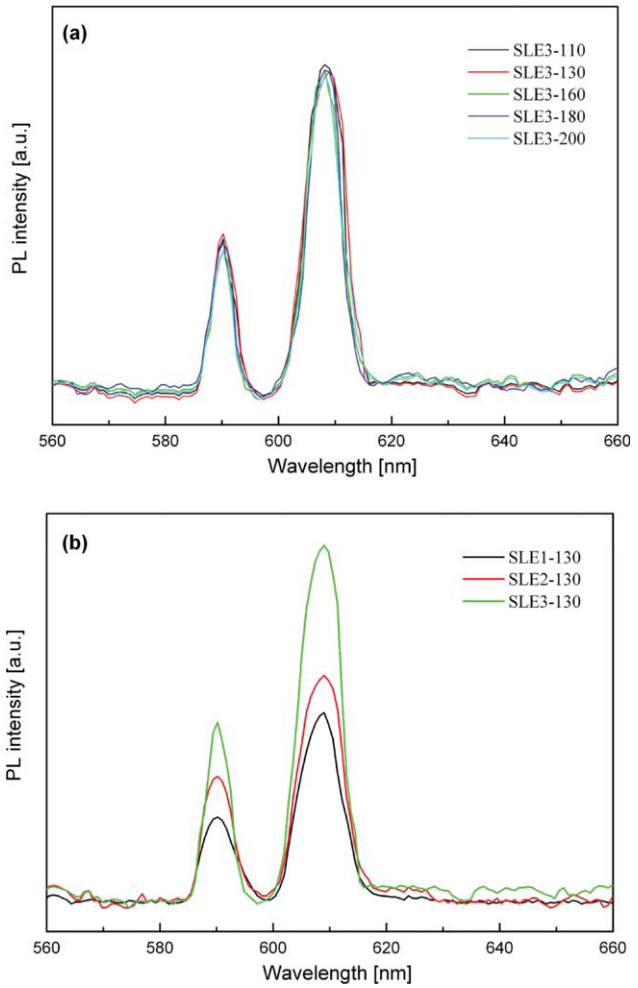

Figure 15. Emission spectra of calcined samples of (a) SLE assembled at different set temperatures; (b) SLE with different Eu contents.

[Color figure can be viewed in the online issue, which is available at wileyonlinelibrary.com.]

Conclusion

A MFJSD equipped with a specially designed micro-fluidic-aerosol-nozzle as a monodisperse droplet generator was used to generate uniform, discrete microparticles with distinctive morphology. With this novel assembly system, characteristics such as particle size, morphology, and structure could be easily controlled by adjusting the precursor compositions and concentrations, initial droplet size, and the drying temperature profile. Examples here were given on pure lactose particles with spherical morphologies, while addition of suspended silica nanoparticles produced composites with bowl-like shapes. Doping europium onto the composites resulted in homogeneous distribution of nano-sized europium oxide particles within the surface (after calcination). The photoluminescence intensity could be enhanced by increasing the initial Eu(III) concentration in the precursors. Unlike spray pyrolysis, the drying temperatures at which the particles were assembled did not affect the distribution of the europium on the structure and thus the photoluminescence spectra. The work here demonstrates a new route to

produce complex composites with uniform properties. Potential applications include assembling heat sensitive or bioactive materials at relatively low temperature synthesis.

Acknowledgments

The authors thank the Australian Research Council Discovery Program for the financial support to this project. W. Wu, R. Amelia, and N. Hao acknowledge Monash Research Graduate School and Department of Chemical Engineering, Monash University for postgraduate scholarships.

Literature Cited

1. Wakefield G, Keron HA, Dobson PJ, Hutchison JL. Synthesis and properties of sub-50-nm europium oxide nanoparticles. *J Coll Int Sci*. 1999;215:179–182.
2. Cheng BC, Wang ZG. Synthesis and optical properties of europium-doped ZnS: long-lasting phosphorescence from aligned nanowires. *Adv Func Mater*. 2005;15:1883–1890.
3. Chen W, Joly AG, Kowalchuk CM, Malm J-O, Huang Y, Bovin J-O. Structure, luminescence, and dynamics of Eu_2O_3 nanoparticles in MCM-41. *J Phys Chem B*. 2002;106:7034–7041.
4. Bazzi R, Flores-Gonzalez MA, Louis C, Lebbou K, Dujardin C, Brenier A, Zhang W, Tillement O, Bernstein E, Perriat P. Synthesis and luminescent properties of sub-5-nm lanthanide oxides nanoparticles. *J Lumin*. 2003;102–103:445–450.
5. Hirai T, Asada Y, Komasawa I. Preparation of Y_2O_3:Eu^{3+} nanoparticles in reverse micellar systems and their photoluminescence properties. *J Coll Int Sci*. 2004;276:339–345.
6. Bera P, Aruna ST, Patil KC, Hegde MS. Studies on Cu/CeO_2: a new NO reduction catalyst. *J Catal*. 1999;186:36–44.
7. Epron F, Gauthard F, Barbier J. Catalytic reduction of nitrate in water on a monometallic Pd/CeO_2 catalyst. *J Catal*. 2002;206:363–367.
8. Fally F, Perrichon V, Vidal H, Kaspar J, Blanco G, Pintado JM, Bernal S, Colon G, Daturi M, Lavalley JC. Modification of the oxygen storage capacity of CeO_2-ZrO_2 mixed oxides after redox cycling aging. *Catal Today*. 2000;59:373–386.
9. Vaqueiro P, Lopez-Quintela MA. Influence of complexing agents and pH on Yttrium-iron garnet synthesized by the sol-gel method. *Chem Mater*. 1997;9:2836–2841.
10. Thongmee S, Winotai P, Tang IM. Local field fluctuations in the substituted aluminum iron garnets, $Y_3Fe_{5-x}Al_xO_{12}$. *Solid State Commun*. 1999;109:471–476.
11. Cheng Z, Yang H, Yu L, Cui Y, Feng S. Preparation and magnetic properties of $Y_3Fe_5O_{12}$ nanoparticles doped with the gadolinium oxide. *J Magn Magn Matter*. 2006;302:259–262.
12. Kang YC, Park SB, Lenggoro IW, Okuyama K. Gd_2O_3:Eu phosphor particles with sphericity, submicron size and non-aggregation characteristics. *J Phys Chem Solids*. 1999;60:379–384.
13. Jin T, Tsutsumi S, Deguchi Y, Machida K, Adachi G. Preparation and luminescence characteristics of the europium and terbium complexes incorporated into a silica matrix using a sol-gel method. *J Alloys Compd*. 1997;252:59–66.
14. Kobayashi Y, Imai J, Nagao D, Konno M. Fabrication of Eu-coated silica particles by homogeneous precipitation method. *Coll Sur A: Physicochem Eng Aspects*. 2008;326:109–114.
15. Mahalingam V, Tan M, Munusamy P, Gilroy JB, Raudsepp M, van-Veggel FCJM. Bright blue photo- and electroluminescence from Eu^{2+}-doped GaN/SiO_2 nanocomposites. *Adv Func Mater*. 2007;17:3462–3469.
16. Kang YC, Lenggoro IW, Okuyama K, Park SB. Luminescence characteristics of Y_2SiO_5:Tb phosphor particles directly prepared by the spray pyrolysis method. *J Electrochem Soc*. 1999;146:1227–1230.
17. Rao RP. Preparation and characterization of fine-grain yttrium-based phosphors by sol-gel Process. *J Electrochem Soc*. 1996;143:189–197.
18. Uekawa N, Ueta M, Wu YJ, Kakegawa K. Synthesis of CeO_2 spherical fine particles by homogeneous precipitation method with polyethylene glycol. *Chem Lett*. 2002;31:854–855.
19. Huignard A, Gacoin T, Boilot J-P. Synthesis and luminescence properties of colloidal YVO_4:Eu phosphors. *Chem Mater*. 2000;12:1090–1094.
20. Murase N, Jagannathan R, Kanematsu Y, Kawasaki Y, Tomita A, Yazawa T, Kushida T. Preparation and fluorescence properties of Eu^{3+}-doped strontium chloroapatite nanocrystals. *J Lumin*. 2000;87–89:488–490.
21. Wang W-N, Widiyastuti W, Lenggoro IW, Kim TO, Okuyama K. Photoluminescence optimization of luminescent nanocomposites fabricated by spray pyrolysis of a colloid-solution precursor. *J Electrochem Soc*. 2007;154:J121–J128.
22. Kang YC, Park SB, Lenggoro IW, Okuyama K. Preparation of non-aggregated Y_2O_3:Eu phosphor particles by spray pyrolysis method. *J Mater Res*. 1999;14:2611–2615.
23. Iskandar F, Gradon L, Okuyama K. Control of the morphology of nanostructured particles prepared by the spray drying of a nanoparticle sol. *J Coll Int Sci*. 2003;265:296–303.
24. Iskandar F, Lenggoro IW, Xia B, Okuyama K. Functional nanostructured silica powders derived from colloidal suspensions by sol spraying. *J Nanopart Res*. 2001;3:263–270.
25. Wu WD, Lin SXQ, Chen XD. Monodisperse droplets formation by Newly designed glass nozzles. *AIChE J*. In press. DOI: 10.1002/aic.12364.
26. Rayleigh L. On the stability of jets. *P Lond Math Soc*. 1878;10:4–13.
27. Lechuga-Ballesteros D, Bakri A, Miller DP. Microcalorimetric measurement of the interactions between water vapor and amorphous pharmaceutical solids. *Pharm Res*. 2003;20:308–318.
28. Vehring R, Foss WR, Lechuga-Ballesteros D. Particle formation in spray drying. *J Aerosol Sci*. 2007;38:728–746.
29. Tsapis N, Dufresne ER, Sinha SS, Riera CS, Hutchinson JW, Mahadevan L, Weitz DA. Onset of buckling in drying droplets of colloidal suspensions. *Phys Rev Lett*. 2005;94:018302.
30. Sugiyama Y, Larsen RJ, Kim J-W, Weitz DA. Buckling and crumpling of drying droplets of colloid-polymer suspensions. *Langmuir*. 2006;22:6024–6030.
31. Pauchard L, Couder Y. Invagination during the collapse of an inhomogeneous spheroidal shell. *Europhys Lett*. 2004;66:667–673.
32. Chen XD, Lin SXQ. Air drying of milk droplet under constant and time-dependent conditions. *AIChE J*. 2005;51:1790–1799.
33. Yao J, Kuang Lim L, Xie J, Hua J, Wang C-H. Characterization of electrospraying process for polymeric particle fabrication. *J Aerosol Sci*. 2008;39:987–1002.
34. Tsapis N, Bennett D, Jackson B, Weitz DA, Edwards DA. Trojan particles: large porous carriers of nanoparticles for drug delivery. *PNAS*. 2002;99:12001–12005.
35. Neely WB. Infrared spectra of carbohydrates. *Adv Carbohydr Chem*. 1957;12:13–33.
36. Otsuka M, Ohtani H, Kaneniwa N, Higuchi S. Isomerization of lactose in solid-state by mechanical stress during grinding. *J Pharm Pharmacol*. 1991;43:148–153.
37. Spedding H. Infrared spectroscopy and carbohydrate chemistry. *Adv Carbohydr Chem*. 1964;19:23–49.
38. Serra J, Gonzále P, Liste S, Serra C, Chiussi S, León B, Pérez-Amor M, Ylänen HO, Hupa M. FTIR and XPS studies of bioactive silica based glasses. *J Non Cryst Solids*. 2003;332:20–27.
39. Sigoli FA, Davolos MR, Jafelicci M. Red and blue emissions of europium doped gadolinium silicate from porous silica matrix and hydroxide carbonate with spherical shaped particles. *J Alloys Comp*. 2002;344:308–311.
40. Pang ML, Lin J, Fu J, Xing RB, Luo CX, Han YC. Preparation, patterning and luminescent properties of nanocrystalline Gd_2O_3:A (A = Eu^{3+}, Dy^{3+}, Sm^{3+}, Er^{3+}) phosphor films via Pechini sol-gel soft lithography. *Opt Mater*. 2003;23:547–558.
41. Yi SS, Bae JS, Moon BK, Jeong JH, Kim JH. Crystallinity of Li-doped Gd_2O_3:Eu^{3+} thin-film phosphors grown on Si (100) substrate. *Appl Phys Lett*. 2005;86:071921–071923.

Manuscript received July 8, 2010, revision received Sept. 6, 2010, and final revision received Oct. 29, 2010.